Field-Driven Hopping Transport of Oxygen Vacancies in Memristive Oxide Switches with Interface-Mediated Resistive Switching

Nan Du,[1,*] Niveditha Manjunath,[1,‡] Yuan Li,[1] Stephan Menzel,[2] Eike Linn,[3] Rainer Waser,[2,3]
Tiangui You,[1] Danilo Bürger,[1] Ilona Skorupa,[1,4] Damian Walczyk,[5,§] Christian Walczyk,[5]
Oliver G. Schmidt,[1,6] and Heidemarie Schmidt[1,7,†]

[1] *Material Systems for Nanoelectronics, Chemnitz University of Technology, 09126 Chemnitz, Germany*
[2] *Peter Grünberg Institut (PGI-7), Forschungszentrum Jülich, 52425 Jülich, Germany*
[3] *Institut für Werkstoffe der Elektrotechnik (IWE 2), RWTH Aachen University, 52066 Aachen, Germany*
[4] *Institute of Ion Beam Physics and Materials Research, Helmholtz-Zentrum Dresden-Rossendorf, 01314 Dresden, Germany*
[5] *Leibniz-Institut für Innovative Mikroelektronik, 15236 Frankfurt/Oder, Germany*
[6] *Institute for Integrative Nanosciences, IFW Dresden, 01069 Dresden, Germany*
[7] *Leibniz Institute for Photonic Technologies (IPHT), 07745 Jena, Germany*

(Received 27 May 2017; revised manuscript received 26 July 2018; published 9 November 2018)

We investigate the hopping transport of positively charged mobile oxygen vacancies V_o^+ in electroforming-free bipolar memristive $BiFeO_3$ switches by conducting impedance spectroscopy and quasistatic state-test measurements. We demonstrate that $BiFeO_3$ switches with mobile oxygen vacancies (V_o^+) and fixed substitutional Ti^{4+} donors on Fe^{3+} lattice sites close to the bottom electrode have a rectifying top electrode with an unflexible barrier height and a rectifying and/or nonrectifying bottom electrode with a flexible barrier height. The field-driven hopping transport of the oxygen vacancies determines the reconfiguration of the flexible barrier and the dynamics of the resistive switching. Average activation energies of 0.53 eV for trapping and of 0.31 eV for the release of oxygen vacancies by the Ti^{4+} donors during application of the SET and RESET excitation pulses are extracted, respectively. The larger activation energy during SET is experimentally verified by impedance spectroscopy measurements and evidences the local enhancement of the electrostatic potential profile at the bottom electrode due to the Ti^{4+} donors on Fe^{3+} lattice sites.

DOI: 10.1103/PhysRevApplied.10.054025

I. INTRODUCTION

The thriving development of memristive oxide devices is arousing interest in the field-enhanced hopping transport of oxygen vacancies not only because in many *n*-type oxides, oxygen vacancies effectively act as double donors [1–3], but also, more importantly, because memristive oxide devices exhibit ultranonlinear switching dynamics [4–6]. Optimized performance requires resistive switching (SET and RESET) within tens of nanoseconds upon the application of a writing bias, and the *on* and *off* resistance states should remain stable for up to 10 years. Field-accelerated ion mobility constitutes one such source of ultranonlinearity [7,8]. The Mott-Gurney nonlinear-ionic-drift model [9] can be employed to interpret the effect of an electric field on the nonlinear rate of ion transport. For instance, the nonlinearity of field-accelerated ion mobility in rutile TiO_{2-x}, which has been studied in a one-dimensional ionic-drift model, causes an observed extremely wide range of lifetime volatility and switching speed in memristive oxide devices [10]. The resistive switching of the *n*-type conducting perovskite $BiFeO_3$ switches depends strongly on the presence of traps for oxygen vacancies and on the concentration of oxygen vacancies and has been described with the ferroelectric model [11] or with the oxygen-vacancy-migration model [12].

In this work, we investigate field-driven hopping transport in a memristive Au/$BiFeO_3$ (BFO)/Pt/Ti metal-oxide-metal switch, because, first of all, the nonlinear oxygen-vacancy drift has been only recently experimentally confirmed using a quasistatic state-test protocol [6]. Second, memristive BFO switches possess

*nan.du@s2012.tu-chemnitz.de
†Heidemarie.Schmidt@etit.tu-chemnitz.de
‡Current affiliation: AIT Austrian Institute of Technology GmbH, Giefinggasse 4, 1210 Vienna, Austria
§Current affiliation: Infineon Technologies AG, Max-Planck-Str. 5, D-59581 Warstein, Germany

 © 2018 American Physical Society

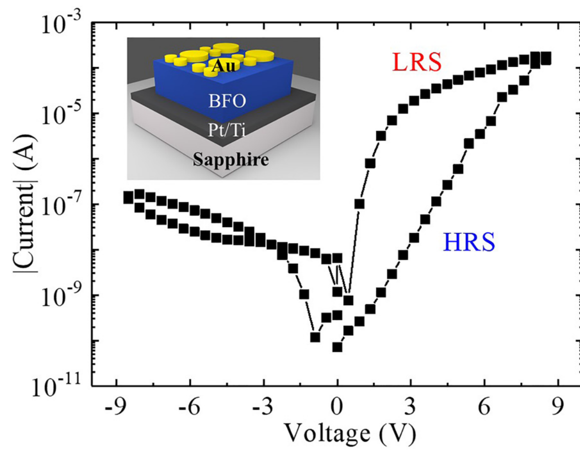

FIG. 1. *I*-*V* characteristics of a $BiFeO_3$ single layer on an unstructured $Pt/Ti/SiO_2/Si$ bottom electrode with a Au contact area of 0.1 mm^2, which has been grown by pulsed-laser deposition. The low-resistance state (LRS) and the high-resistance state (HRS) are written by applying a 10-ms-long bias pulse with an amplitude of +8.5 V and −8.5 V, respectively. The inset shows a schematic sketch of the BFO memristive switch.

excellent bipolar switching performance [12], including a long retention time and stable endurance even at elevated temperatures. Ferroelectric switching can be excluded from polarization–electric-field (*P*-*E*) measurements on the Au/BFO/Pt/Ti memristors where we ramp the bias amplitude in the same bias range as used to demonstrate the resistive-switching behavior (Fig. 1). Furthermore, due to the interface-mediated resistive switching, memristive BFO switches reveal negligible Joule heating and electroforming-free resistive switching. Thus, the measured increase in mobility of oxygen vacancies can be attributed unambiguously to the field enhancement rather than to temperature enhancement.

II. IMPEDANCE OF BFO MEMRISTIVE DEVICES

Polycrystalline perovskite structure (R3c space group) BFO films are grown by pulsed-laser deposition (PLD) on a Pt/Ti bottom electrode (approximately 190 nm) on SiO_2/Si substrates. The BFO films, with a nominal thickness of 600 nm, are deposited at 650 °C under an oxygen partial pressure of 9.75 mTorr. Note that the BFO thickness can be scaled down to 100–300 nm [13]. Oxygen vacancies V_o^+ are intrinsically formed during PLD growth of the film. Thus, the obtained BFO films can be considered as a *n*-type semiconductor. Approximately 180-nm-thick Au top electrodes with an area of 0.1 mm^2 are deposited onto BFO thin films by dc sputtering for subsequent resistive-switching measurements.

The investigated BFO switch has a Pt/Ti bottom electrode with a flexible barrier height. Therefore, hysteresis is observed in the positive bias range. Typically, the SET/RESET bias with an amplitude of +7/−7 V and a pulse width of 100 ms are used. The SET and RESET excitation pulses are extracted from *I*-*V* characteristics that are ramped with bias in steps of 0.36 V and with a sweeping velocity of 0.36 V per 100 ms. The amplitude of the current is plotted on a logarithmic scale as shown in Fig. 1. Schottky-like barriers are formed at the Au-BFO and BFO-Pt interfaces [14]. In previous studies, we have shown that the Pt/Ti bottom electrode in memristive BFO switches forms a rectifying or nonrectifying contact with a flexible barrier height by the bias-driven forward-backward migration of oxygen vacancies [12] and by the trapping and release of oxygen vacancies by fixed substitutional Ti^{4+} donors on Fe^{3+} lattice sites [15]. As shown by Yang *et al.* [16], substitutional doping will work if the ionic radius of the dopant ion is comparable to the ionic radius of the replaced ion. Yang *et al.* give an overview on possible substitutional dopants in the perovskite $BiFeO_3$ on A-sites (Bi^{3+}), e.g., Pb^{2+}, Ba^{2+}, Ca^{2+} and Ce^{4+}, and on *B*-sites (Fe^{3+}), e.g., Ti^{4+}, Mn^{4+}, Zr^{4+} and Cr^{2+}. The ionic radius of Ti^{4+} is comparable to that of Fe^{3+} in the $BiFeO_3$ perovskite structure. Ti^{4+} is a donor because it replaces Fe^{3+}. In a previous work, we have investigated the substrate effect on the resistive switching in $BiFeO_3$ thin films and have shown that there is no resistive switching in $BiFeO_3$ without Ti doping [17]. In this work, we conduct temperature-dependent impedance spectroscopy and quasistatic state-test measurements in order to investigate the hopping-transport properties of oxygen vacancies, e.g., the activation energy, ac conductivity, and carrier mobility. From the extracted activation energy, we conclude that the mobile oxygen vacancies and fixed substitutional Ti donors close to the bottom electrode locally change the electrostatic profile and play the leading role in the reconfiguration of the barrier at the bottom electrode during SET and RESET in BFO.

Impedance data are used to determine the parameters of the BFO switch in the LRS and the HRS of a equivalent circuit built from elements *R*, *C*, *L*, and the constant-phase element (CPE). Schottky barriers form depletion layers and are described in a first approximation by the elements *R* and *C* on the length scale of the depletion layer. The modeled elements *C* can be related to the Schottky barriers of the metal electrodes, which form a depletion layer at the interface between the metal electrodes and BFO bulk layer. Nyquist data are recorded by applying a 10 mV ac small-signal frequency sweep from 0.01 to 10 Hz at 298, 323, and 348 K (Fig. 2). To permit a valid analysis of the full-frequency response, we employ an equivalent-circuit model with two CPEs for the LRS with a rectifying top and nonrectifying bottom interface [insets in Figs. 2(a) and 2(c)] and for the HRS with a rectifying

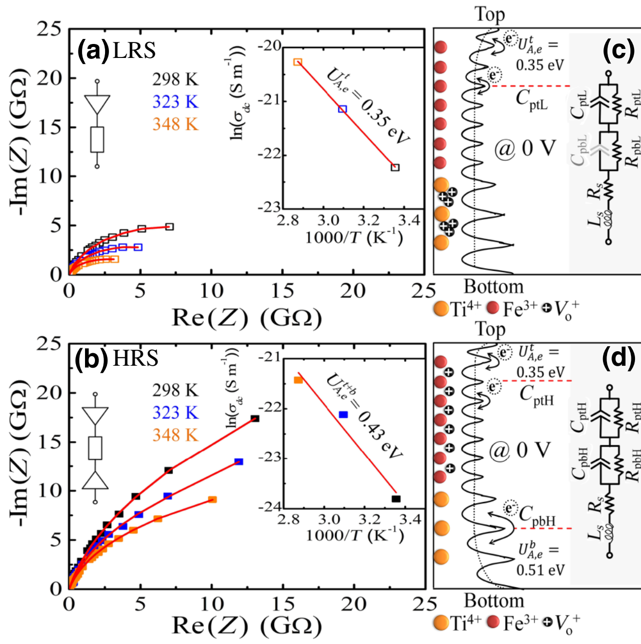

FIG. 2. Measured (symbols) and modeled (lines) Nyquist plots of a memristive BFO switch in (a) the LRS and (b) the HRS at 298 K, 323 K, and 348 K. $\ln(\sigma_{dc})$ versus $1000/T$ plots are shown as insets. A schematic representation of the potential profile and superimposed electrostatic potential at zero dc bias at the position of Fe^{3+} (red circles) and Ti^{4+} (orange circles) (c) in the LRS with a single depletion layer with extension d_t and (d) in the HRS with two depletion layers with extension d_t and d_b. The arrows illustrate ac hopping transport of electron charges at the end of the depletion layer. Corresponding equivalent circuits are shown on the right-hand side.

top and rectifying bottom interface as a head-to-head rectifier, which consists of two antiserially connected diodes [insets in Figs. 2(b) and 2(d)]. The CPE is a good approximation with which to model the BFO memristive switch as an imperfect capacitor. The series resistance R_s and the parasitic inductance L_s account for the influence of the electrodes on the real and imaginary parts of the complex impedance Z^*. The impedance of the equivalent circuit is given by

$$Z^*(\omega) = [R_{pt}^{-1} + i\omega C_{pt}]^{-1} + [R_{pb}^{-1} + i\omega C_{pb}]^{-1} + R_s + i\omega L_s. \quad (1)$$

Note that the diameter of the impedance semicircle scales with the bulk resistance R_p. C_{pt} and C_{pb} denote the bulk capacitance of the depletion layers at both top and bottom interface of bismuth ferrite, respectively. Measured and modeled impedance spectra along with the corresponding equivalent circuit are shown for the LRS [Fig. 2(a)] and for the HRS [Fig. 2(b)]. With increasing temperature, the depletion-layer extension of C_{pt} and C_{pb} increases and the impedance semicircle is distorted. Namely, R_p decreases with increasing temperature, as is expected for an increasing concentration of majority carriers with increasing temperature. Based on the equivalent circuit, the model parameters C_p, R_p, R_s, and L_s are derived and listed in Table I. C_{pt} possesses the same temperature dependence in both the LRS and the HRS and is marked as the depletion-layer bulk capacitance at the top electrode. In the HRS, the accumulation of oxygen vacancies near the Au-BFO interface decreases the extension of the top depletion layer and thus causes the observed increase of the bulk capacitance C_{pt} in both the LRS (C_{ptL}) and the HRS (C_{ptH}) with increasing temperature. However, as expected, the C_{ptL} is larger than the overall capacitance in the HRS due to the antiserial connection between C_{ptH} and C_{pbH}, which is in agreement with experimental capacitance-voltage measurements on memristive BFO switches at zero dc bias [18]. The negligible influence of C_{pbL} and R_{pbL} proves that in the LRS, the bottom electrode is nonrectifying.

To illustrate the contribution of band carriers and the space-charge region, next we move from the electrical modeling to the physical modeling. It should be noted that purely electronic processes and geometry effects can

TABLE I. The modeled parallel capacitance C_p, parallel resistance R_p, series resistance R_s, and parasitic inductance L_s of a $BiFeO_3$ memristive switch in the LRS and the HRS at 298, 323, and 348 K: "t" and "b" refer to top and bottom, respectively. The barrier height $\Phi_{B\eta}$ and the ideality factor η are been fitted using Eq. (2) from the temperature-dependent I-V characteristics in the LRS. The relative permittivity ϵ_r in the LRS (bold), the top-depletion-layer thickness d_t and the bottom-depletion-layer thickness d_b in the HRS (bold) are calculated using the relation $d = \epsilon_0 \epsilon_r A / C_p$, Eq. (3), the barrier height $\Phi_{B\eta}$, and the ideality factor η. The temperature-dependent dc conductivity σ_{dc} is extracted using Eq. (4).

	T (K)	C_{pt} (nF)	C_{pb} (nF)	R_{pt} (GΩ)	R_{pb} (GΩ)	R_s (Ω)	L_s (mH)	η (1)	$\Phi_{B\eta}$ (eV)	$\boldsymbol{\epsilon_r}$ (1)	d_t (nm)	$\boldsymbol{d_b}$ (nm)	σ_{dc} ($\times 10^{-10}$ Ω^{-1}m^{-1})
	298	0.90	⋯	13.80	1.93×10^{-9}	0.08	11.8	3.5	0.94	**52**	51.2	⋯	2.21
LRS	323	1.01	⋯	8.53	1.84×10^{-9}	0.05	15.4	3.4	1.02	**72**	62.6	⋯	6.59
	348	1.39	⋯	4.83	1.50×10^{-9}	0.07	11.3	3.2	1.09	**145**	92.1	⋯	15.75
	298	1.11	1.04	55.18	10.22	0.06	2.3	⋯	⋯	⋯	41.4	**44.0**	0.46
HRS	323	1.14	0.94	33.71	6.11	0.07	3.5	⋯	⋯	⋯	55.5	**61.6**	2.48
	348	1.56	0.87	21.32	5.87	0.05	3.4	⋯	⋯	⋯	82.0	**147.8**	4.95

be extracted only from frequency-dependent impedance data in the gigahertz frequency range [19]. First, following work presented in [12], we fit the temperature-dependent barrier height $\phi_{B\eta}$ and the ideality factor η from the temperature-dependent I-V characteristics in the LRS by using the Shockley equation [20], as follows:

$$I = AA^{*}T^{2}\exp\left(-\frac{e\phi_{B\eta}}{k_B T}\right)\left\{\exp\left[\frac{e(V-IR_{ss})}{\eta k_B T}\right]-1\right\} + \frac{V-IR_{ss}}{R_{pp}}, \tag{2}$$

where A is the area of the diodes, A^{*} is the effective Richardson constant, $\phi_{B\eta}$ is the barrier height, η is the ideality factor, R_{ss} is the series resistance, and R_{pp} is the parallel resistance. By combining the relationship $d = \epsilon_0\epsilon_r A/C_p$ with the barrier-height-dependent depletion-layer width d [21]

$$d = \sqrt{\frac{2\epsilon_0\epsilon_r(\phi_{B\eta}/e - V_t - k_B T/e)}{en}}, \tag{3}$$

and using the barrier height $\phi_{B\eta}$ in the LRS (Table I), we calculate the relative permittivity ϵ_r as a function of the temperature. Side effects, e.g., pinning by defects and metal quality, are included by the ideality factor η in Eq. (2). Here, V_t, e, ϵ_0, and n are the top electrode bias (0 V), the electron charge, the vacuum permittivity, and the intrinsic charge-carrier density of oxygen defects ($n = 2\times10^{18}$ cm^{-3}), respectively. k_B and T have their usual meanings. The computed ϵ_r values amount to 52, 72, and 145, i.e., ϵ_r increases with increasing temperature (Table I), which is in agreement with Ref. [22], where ϵ_r of BFO is reported to increase with increasing temperature. We further use the ϵ_r values to calculate the extension d_t of the depletion layer in the LRS and the extensions d_t and d_b of the depletion layer in the HRS. Thus the depletion-layer extension d can be calculated from Eq. (3). The superimposed electrostatic potential at zero bias, which demonstrates recognizable depletion layers d_t in the LRS [Fig. 2(c)] and d_t and d_b in the HRS [Fig. 2(d)], is calculated by performing 2D electrostatic calculations using COMSOL Multiphysics. The electrostatic potential profile is shown in Fig. 3. Note that for the LRS the built-in potential is developed only at the end of the top depletion layer d_t, whereas for the HRS it is developed at the ends of both the top and bottom depletion layers d_t and d_b.

We further extract the frequency-dependent conductivity of the small signal frequency from impedance spectroscopy. The total conductivity σ^{*}_{tot} is given as follows [23,24]:

$$\sigma^{*}_{\text{tot}}(\omega) = \sigma_{\text{dc}} + i\omega\epsilon_0\epsilon^{*}_r(\omega), \tag{4}$$

with frequency-dependent complex permittivity $\epsilon^{*}_r(\omega) = 1/(i\omega C_0 Z^{*}(\omega))$, where σ_{dc} is the dc conductivity due to band conduction, and the ac conductivity is due to relaxation processes caused by the motion of electrons. C_0 is the geometrical capacitance of the memristive BFO switch. The dc conductivity σ_{dc} as listed in Table I is obtained by extending the total conductivity σ^{*}_{tot} to zero frequency. The Arrhenius equation [25,26],

$$\sigma_{\text{dc}} = \sigma_0\exp(-U_{A,e}/k_B T), \tag{5}$$

is used to derive the activation energy $U_{A,e}$ as depicted in the insets of Figs. 2(a) and 2(b). σ_0 is the pre-exponential factor. If the temperature is increased from 298 to 348 K, the dc conductivity is increased by a factor of 7 in the LRS and by a factor of 10 in the HRS. Despite this small variation in the dc conductivity, we use Eq. (5) and approximate the activation energy $U^{t}_{A,e} = 0.35$ eV of hopping electron

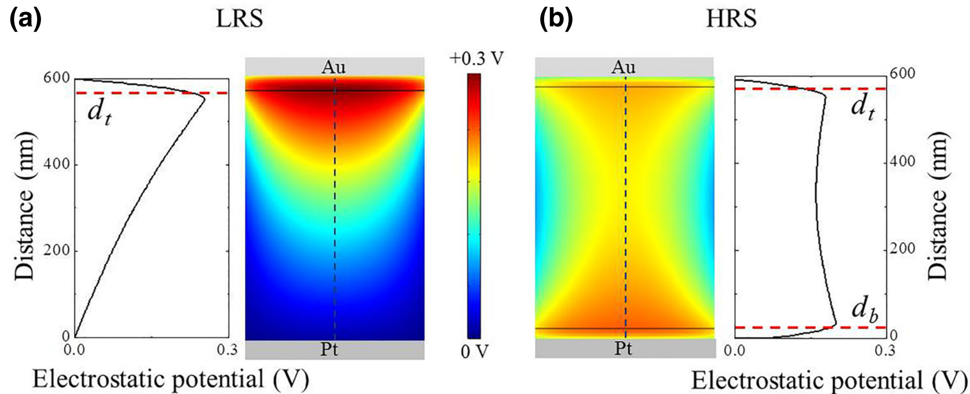

FIG. 3. Electrostatic potential 2D images and profiles in a BFO switch with a Au top electrode and a Pt bottom electrode (a) in the LRS with corresponding depletion layer d_t and (b) in the HRS with corresponding depletion layers d_t and d_b by using the computational software COMSOL Multiphysics at zero dc bias. The color scale represents the amplitude of electrostatic potential. The red scattered lines in the mapping images indicate the end of the top (d_t) and bottom (d_b) depletion layers and the electrostatic potential profile is represented by black solid lines.

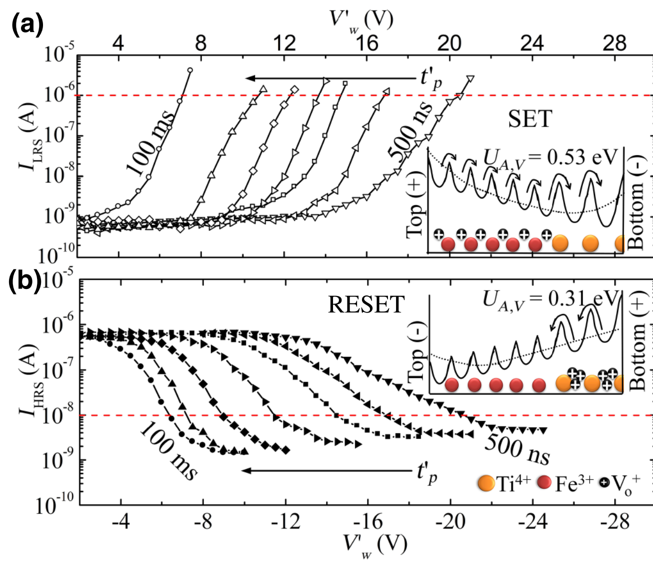

FIG. 4. The quasistatic state-test protocol with different pulse widths t'_p (100 ms, 10 ms, 1 ms, 100 μs, 10 μs, 1 μs, and 500 ns) and excitation amplitudes V'_w during (a) SET and (b) RESET. The insets show the schematics of the potential profile and the superimposed electrostatic potential under applied dc bias at the position of Fe^{3+} (red colors) and of Ti^{4+} (orange circles) with writing pulses (a) $V'_w = +7$ V and (b) $V'_w = -7$ V. The arrows illustrate the field-driven hopping transport of the oxygen vacancies.

charges at the end of the single depletion layer d_t in the LRS and the activation energy $U^{t+b}_{A,e} = 0.43$ eV, respectively. $U^{t+b}_{A,e}$ is the mean value of the activation energy of hopping electron charges at the ends of both depletion layers d_t and d_b in the HRS; thus $U^{b}_{A,e} = 0.51$ eV. It can be concluded that in addition to the local change of electrostatic potential by Ti^{4+} donors on Fe^{3+} lattice sites, the electrostatic potential for bulk transport is also modulated in the presence of band bending close to both electrodes. We analyze the frequency-independent impedance data to extract the dc conductivity. In a first approximation, we assume that band-bending effects in the depletion layers are superimposed with the potential profile on the atomistic scale, which varies due to the constituents of the BFO lattice, and determine the activation energy of the hopping transport properties on the atomistic scale.

III. DYNAMICS OF BFO MEMRISTIVE DEVICES

In the following, we discuss the quasistatic state-test protocol [6] executed at five different temperatures, in order to investigate the field-driven hopping transport of oxygen vacancies in BFO. It is expected that the mobility during RESET exceeds that during SET due to the preferred equilibrium distribution of oxygen vacancies and different band bending in the HRS and in the LRS close to the bottom electrodes, as illustrated in the insets in Fig. 4. Because we cannot directly visualize the distribution of oxygen vacancies after application of an excitation amplitude V'_w during SET [Fig. 4(a)] and RESET [Fig. 4(b)], we analyze the read-out currents I_{LRS} in the LRS and I_{HRS} in the HRS. The read-out current is a measure of the change of the electrostatic profile in the LRS and the HRS due to the distribution of oxygen vacancies. In order to illustrate the band bending during application of a bias, the electrostatic potential in BFO under the applied SET and RESET bias is calculated using COMSOL Multiphysics. The amplitude and direction of the electrostatic potential between the top and bottom electrodes is shown in Fig. 5. It reveals that the applied bias drops over the whole length of the BFO memristive switch and that the potential, which is superimposed from the applied bias and the depletion-layer potential without applied bias (Fig. 3), mainly drops over the bottom depletion layer d_b during SET [Fig. 5(a)] and over the top depletion layer d_t during RESET [Fig. 5(b)]. The quasistatic state-test protocol (Fig. 4) starts with initializing the BFO into the HRS (LRS) by a negative (positive) initialization pulse with amplitude $V_w = -7$ V$/+7$ V and with pulse width $t_p = 100$ ms. Different pairs of excitation pulses V'_w up to +21 V for SET and down to −24 V for RESET and pulse widths t'_p in the range from 100 to 500 ns are tested. The distinct behavior is observed from the current I_{LRS} in the LRS and from the current I_{HRS} in the HRS. I_{LRS} and I_{HRS} depend strongly on the excitation-pulse amplitude and pulse width,

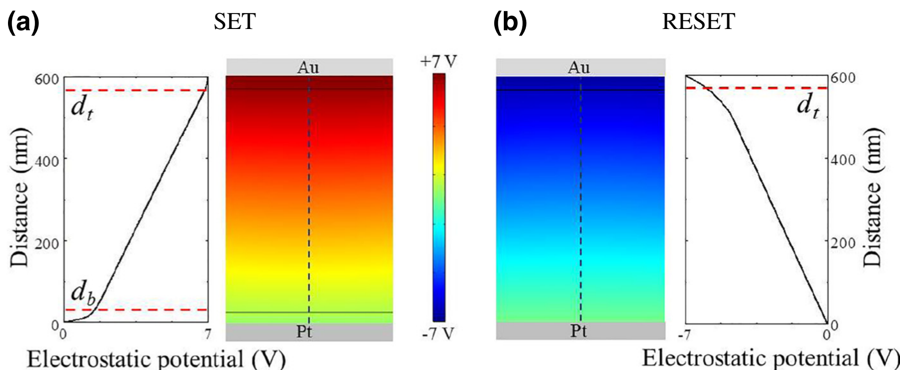

FIG. 5. Electrostatic-potential 2D images and profiles in a BFO switch with a Au top electrode and a Pt bottom electrode under applied bias (a) in SET with corresponding depletion layers d_t and d_b and (b) in RESET with corresponding depletion layer d_t calculated using COMSOL Multiphysics. The color scale represents the magnitude of the electrostatic potential. The red scattered lines in the 2D images indicate the ends of the top and bottom depletion layers.

as demonstrated in Fig. 4. When reducing the excitation-pulse amplitude by a factor of 5, the pulse width t'_p has to be increased by more than 6 orders of magnitude in order to realize resistive switching. This result proves the extremely large nonlinearity of the switching kinetics in memristive BFO switches. We use the Mott-Gurney ionic-drift model [9] to analyze the drift of oxygen vacancies in the presence of substitutional Ti traps at five different temperatures. Here, it is assumed that ions of charge z jump between neighboring sites in a one-dimensional periodic lattice by surmounting an activation barrier $U_{A,V}$, as illustrated in Fig. 4. The drift velocity v_d of oxygen vacancies V_{o}^{+} is derived from the rigid point-ion model and is given as follows:

$$v_d = fa \exp\left(\frac{-U_{A,V}}{k_B T}\right) \sinh\left(\frac{|z|eaE'}{k_B T}\right), \tag{6}$$

where z is the charge number ($z = 1$), f is the frequency of escape attempts, and a is the distance between the initial and the saddle-point configuration of the hopping oxygen vacancies. Thus, the mobility of oxygen vacancies can be calculated from $\mu_d = v_d/E'$. According to the hyperbolic-sine approximation, if $E' \ll E_0 = (k_B T)/(|z|ea)$, i.e., in the linear regime of Eq. (6), it leads to the following expression for the mobility μ_d of the oxygen vacancies in the small-field case ($E' \ll E_0$):

$$\mu_d = \frac{|z|efa^2 \exp[-U_{A,V}/(k_B T)]}{k_B T}, \tag{7}$$

where E_0 is the characteristic electric field. Note that the barrier height of the bottom electrode will only reduce from rectifying to nonrectifying if enough image charges are built up in the bottom electrode as mobile oxygen vacancies approach the bottom electrode–$BiFeO_3$ interface. The largest possible number of oxygen vacancies that can cause the observed barrier-height lowering are all oxygen vacancies driven by the electric field E' in the volume between the top and bottom electrodes. This field strength is determined by $E' = V'_w/L$, where L is the thickness of the BFO thin film. The examined field strengths amount to $0.04 < |E'|/\mathrm{MVcm}^{-1} < 0.44$ for SET and $0.06 < |E'|/\mathrm{MVcm}^{-1} < 0.35$ for RESET, as shown in Figs. 6(a) and 6(b), respectively. The tested field strengths lie in the range where $E' \geq E_0$ and where the Mott-Gurney ionic-drift model predicts an exponential increase in ion mobility [9].

The migration and redistribution of oxygen vacancies in SET and RESET drives the interface-mediated resistive switching in the electroforming-free bipolar memristive $BiFeO_3$ switches. The drift velocity of the oxygen vacancies v_d during the resistive switching through a BFO film of thickness L can be denoted as $v_d = L/t'_p$ [8]. Note that v_d, L, and E' are aligned with (+) and are opposite to (−)

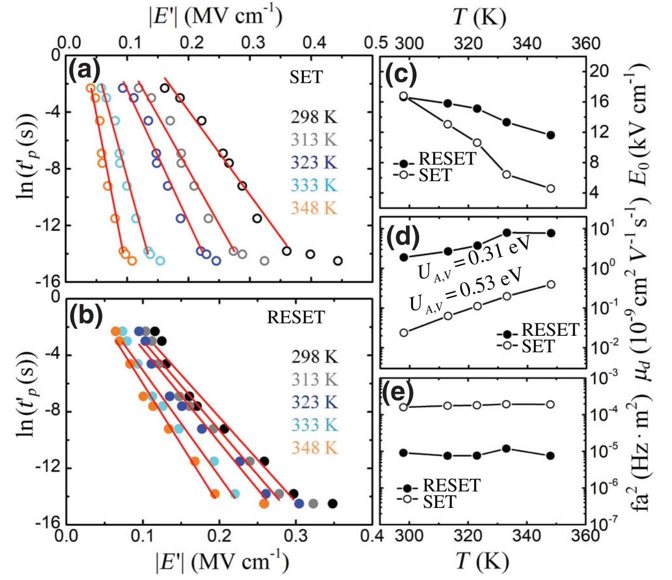

FIG. 6. Experimental (symbols) and modeled (lines) (E', t'_p) pairs from quasistatic state-test measurements at 298, 313, 323, 343, and 348 K, plotted as $\ln(t'_p)$ versus $|E'|$ (a) in SET with $I_{\mathrm{LRS}} = 10^{-6}$ A and (b) in RESET with $I_{\mathrm{HRS}} = 10^{-8}$ A. The extracted (c) characteristic field E_0 and (d) mobility μ_d, and (e) the product of fa^2 are plotted versus temperature.

the direction of the electric field during the applied writing bias. By rearranging Eq. (6) into the form $t'_p = L/v_d$, we obtain the exponential dependence of the pulse widths t'_p on the applied electric field E':

$$\ln(t'_{p,\mathrm{SET/RESET}}) = \ln\left(\pm\frac{2L}{E_0 \mu_d}\right) \mp \frac{E'}{E_0}. \tag{8}$$

The agreement between the experimental and modeled (E', t'_p) pairs, as shown in Fig. 6(a) for SET and Fig. 6(b) for RESET, implies that the voltage-time dilemma is resolved in memristive BFO switches. That is because of the exponential increase of the oxygen-vacancy drift velocity with the linearly increasing electric field. The characteristic electric field E_0 is extracted from the slope of $\ln(t'_p)$ versus E'. The E_0 values [Fig. 6(c)] suggest that the examined field strengths $|E'|$ lie in the valid range of the Mott-Gurney ionic-drift model ($E' \geq E_0$). The drift mobility μ_d in RESET is around 2 orders of magnitude larger than μ_d in SET at room temperature [Fig. 6(d)] The activation energy can be estimated from the slope of the representation of $\ln(\mu_d T)$ versus $1/T$ and amounts to 0.31 eV in RESET and 0.53 eV in SET. By way of explanation, it is easier to release oxygen vacancies from Ti traps during RESET than to trap oxygen vacancies by Ti traps during SET. The agreement between the activation energy for hopping transport of oxygen vacancies V_{o}^{+} during SET ($U_{A,V} = 0.53$ eV) and the activation energy of hopping

electrons e at the end of the depletion layer at the bottom electrode ($U^{b}_{A,e} = 0.51$ eV) proves that in SET the main barrier for hopping transport of oxygen vacancies is formed at the bottom electrode [inset in Fig. 4(a)]. Moreover, the drift mobility in SET increases more significantly with temperature than in RESET and accounts for the observed larger switching speed in SET at elevated temperature. According to the lattice constant of rhombohedral bismuth ferrite (0.56 nm [27]), the hopping frequency f at room temperature amounts to 2.8×10^{13} Hz in RESET and 5.8×10^{14} Hz in SET, i.e., it lies in the far-infrared frequency range, between 3.0×10^{11} Hz and 4.3×10^{15} Hz [10]. Note that the experimental (E', t'_p) pairs with $t'_p > 1\ \mu$s are leveling off in higher-field-strength ranges in SET and RESET at each temperature, as shown in Figs. 6(a) and 6(b). This is possibly due to an extrinsic effect such as increased bulk capacitance at sufficiently high voltages, which has been observed in most resistive-switching devices. It suggests that in order to realize resistive-switching devices with a switching time down to a few nanoseconds, it is recommended not only to increase the pulse amplitude but also to downscale the characteristic dimensions of the cell.

IV. SUMMARY AND OUTLOOK

In summary, we investigate the field-driven hopping transport of oxygen vacancies in electroforming-free BFO switches with interface-type resistive switching by conducting experimental and modeled temperature-dependent impedance spectroscopy and quasistatic state-test measurements. Due to substitutional Ti traps near the bottom electrode of the memristive BFO switch and mobile oxygen vacancies, a Schottky barrier with a flexible barrier height is formed at the bottom electrode and enables bipolar resistive switching with excellent functional reliability. The hopping transport of oxygen vacancies during SET and RESET determines the dynamics of resistive switching. The modeled activation barriers for hopping transport of oxygen vacancies close to the top and bottom electrodes amount to 0.31 eV in RESET and 0.53 eV in SET. Comparable activation barriers are found for ac transport of electrons by impedance spectroscopy with zero bias. That reflects the electrostatic potential profile in the top depletion region and in the bottom depletion region of memristive BFO switches with substitutional Ti traps in the bottom electrode regions. The extracted smaller activation energy and larger carrier mobility of oxygen vacancies in RESET compared to SET indicate that RESET is faster in memristive BFO switches. The experimental study on the electrostatic potential profile is useful for a quantitative comparison between the experimental and future first-principles computational design of memristive oxide switches with substitutional dopants for trapping and releasing oxygen vacancies.

ACKNOWLEDGMENTS

We are indebted to H. Wylezich, T. Schröder, and R. Patra for fruitful discussions and to S. Slesazeck, B. Max, and T. Mikolajick for help with the *P*-*E* measurements. Financial support by the Fraunhofer Internal Program under Grant No. Attract 134-600768, by the Deutsche Forschungsgemeinschaft (Grants No. LI 2416/1-1, SCHM 1663/4-1,2, and SFB 917) and by the Initiative and Networking Fund of the Helmholtz Association (Grant No. VH-VI-422) made this work possible.

[1] J. He, R. K. Behera, M. W. Finnis, X. Li, E. C. Dickey, S. R. Phillpot, and S. B. Sinnott, Prediction of high temperature point defect formation in TiO_2 from combined *ab initio* and thermodynamic calculations, Acta Mater. **55**, 4325 (2007).

[2] A. Janotti, J. B. Varley, M. Choi, and C. G. Van de Walle, Vacancies and small polarons in $SrTiO_3$, Phys. Rev. B **90**, 085202 (2014).

[3] S. J. Clark and J. Robertson, Energy levels of oxygen vacancies in $BiFeO_2$ by screened exchange, Appl. Phys. Lett. **94**, 022902 (2009).

[4] M. D. Pickett, D. B. Strukov, J. L. Borghetti, J. J. Yang, G. S. Snider, D. R. Stewart, and R. S. Williams, Switching dynamics in titanium dioxide memristive devices, J. Appl. Phys. **106**, 074508 (2009).

[5] F. Messerschmitt, M. Kubicek, S. Schweiger, and J. L. Rupp, Memristor kinetics and diffusion characteristics for mixed anionic-electronic $SrTiO_{3-\delta}$ bits: The memristor-based Cottrell analysis connecting material to device performance, Adv. Funct. Mater. **24**, 7448 (2014).

[6] N. Du, M. Kiani, C. Mayr, T. You, D. Bürger, I. Skorupa, O. G. Schmidt, and H. Schmidt, Single pairing spike-timing dependent plasticity in $BiFeO_3$ memristors with a time window of 25 ms to 125 μs, Front. Neurosci. **9**, 227 (2015).

[7] S. Menzel, M. Waters, A. Marchewka, U. Böttger, R. Dittmann, and R. Waser, Origin of the ultranonlinear switching kinetics in oxide-based resistive switches, Adv. Funct. Mater. **21**, 4487 (2011).

[8] S. Menzel, S. Tappertzhofen, R. Waser, and I. Valov, Switching kinetics of electrochemical metallization memory cells, Phys. Chem. Chem. Phys. **15**, 6945 (2013).

[9] N. F. Mott and R. W. Gurney, *Electronic Processes in Ionic Crystals* (Clarendon Press, Oxford, 1940).

[10] D. Strukov and R. S. Williams, Exponential ionic drift: Fast switching and low volatility of thin film memristors, Appl. Phys. A **94**, 515 (2009).

[11] Y. Lei, H. Z. Zeng, W. B. Luo, Y. Shuai, X. H. Wei, N. Du, D. Buerger, I. Skorupa, J. S. Liu, O. G. Schmidt, W. L. Zhang, and H. Schmidt, Ferroelectric and flexible barrier resistive switching of epitaxial $BiFeO_3$ films studied by temperature-dependent current and capacitance spectroscopy, J. Mater. Sci.: Mater. Electron. **27**, 7927 (2016).

[12] T. You, N. Du, S. Slesazeck, T. Mikolajick, G. Li, D. Bürger, I. Skorupa, H. Stöcker, B. Abendroth, A. Beyer, K. Volz, O. G. Schmidt, and H. Schmidt, Bipolar electric-field enhanced trapping and detrapping of mobile donors

in $BiFeO_3$ memristors, ACS Appl. Mater. Interfaces **6**, 22 (2014).

[13] L. Jin, Y. Shuai, X. Ou, P. F. Siles, H. Z. Zeng, T. You, N. Du, D. Bürger, I. Skorupa, S. Q. Zhou, L. W. Bo., C. G. Wu, W. L. Zhang, T. Mikolajick, O. G. Schmidt, and H. Schmidt, Resistive switching in unstructured, polycrystalline $BiFeO_3$ thin films with downscaled electrodes, Phys. Status Solidi A **211**, 2563 (2014).

[14] C. Ge, K. J. Jin, C. Wang, H. B. Lu, C. Wang, and G. Z. Yang, Numerical investigation into the switchable diode effect in metal-ferroelectric-metal structures, Appl. Phys. Lett. **99**, 063509 (2011).

[15] T. G. You, X. Ou, G. Niu, F. Bärwolf, G. D. Li, N. Du, D. Bürger, I. Skorupa, Q. Jia, W. J. Yu, X. Wang, O. G. Schmidt, and H. Schmidt, Engineering interface-type resistive switching in $BiFeO_3$ thin film switches by Ti implantation of bottom electrodes, Sci. Rep. **5**, 18623 (2015).

[16] C. Yang, D. Kan, I. Takeuchi, V. Nagarajand, and J. Seidel, Doping $BiFeO_3$: Approaches and enhanced functionality, Phys. Chem. Chem. Phys. **14**, 15953 (2012).

[17] Y. Shuai, X. Ou, C. Wu, W. Zhang, S. Zhou, D. Bürger, H. Reuther, S. Slesazeck, T. Mikolajick, M. Helm, and H. Schmidt, Substrate effect on the resistive switching in $BiFeO_3$ thin films, J. Appl. Phys. **111**, 07D906 (2012).

[18] Y. Shuai, S. Q. Zhou, D. Bürger, M. Helm, and H. Schmidt, Nonvolatile bipolar resistive switching in $Au/BiFeO_3/Pt$, J. Appl. Phys. **109**, 124117 (2011).

[19] R. Wilcoxon, The effects of geometry and dielectric material on stripline and microstrip internal temperatures, IEEE Trans. Compon. Packaging Technol. **28**, 674 (2005).

[20] A. Dimoulas, P. Tsipas, A. Sotiropoulos, and E. K. Evangelou, Fermi-level pinning and charge neutrality level in germanium, Appl. Phys. Lett. **89**, 252110 (2006).

[21] M. Grundmann, *The Physics of Semiconductors* (Springer, Heidelberg, 2016).

[22] J. Lu, A. Günther, F. Schrettle, F. Mayr, S. Krohns, P. Lunkenheimer, A. Pimenov, V. D. Travkin, A. A. Mukhin, and A. Loidl, On the room temperature multiferroic $BiFeO_3$: Magnetic, dielectric and thermal properties, Eur. Phys. J. B **75**, 4 (2010).

[23] M. Pollak, On the frequency dependence of conductivity in amorphous solids, Philos. Mag. **23**, 519 (1971).

[24] S. R. Elliott, A.c. conduction in amorphous chalcogenide and pnictide semiconductors, Adv. Phys. **36**, 135 (1987).

[25] V. Saltas, V. Chatzistamou, D. Pentari, E. Paris, D. Triantis, I. Fitilis, and F. Vallianatos, Complex electrical conductivity measurements of a KTB amphibolite sample at elevated temperatures, Mater. Chem. Phys. **139**, 169 (2013).

[26] V. Prakash, A. Dutta, S. Choudhary, and T. Sinha, Dielectric relaxation in perovskite $Ba(Zn_{1/2}W_{1/2})O_3$, Mater. Sci. Eng. B **142**, 98 (2007).

[27] M. M. Kumar, V. R. P. Srinivas, and S. V. Suryanarayana, Ferroeletricity in a pure $BiFeO_3$ ceramic, Appl. Phys. Lett. **76**, 2764 (2000).